photonics

MDPI

Article

High-Order Multipole-Driven Absorption Enhancement in Dielectric Metasurfaces

Pavel Terekhov [1,2,*] and Vladimir Aksyuk [1]

[1] Physical Measurement Laboratory, National Institute of Standards and Technology, Gaithersburg, MD 20899, USA; vladimir.aksyuk@nist.gov
[2] Theiss Research, La Jolla, CA 92037, USA
* Correspondence: pavel.terekhov@nist.gov

Abstract

This work numerically investigates resonantly enhanced absorption in an all-dielectric metasurface composed of crystalline silicon (c-Si) quadrumer clusters. Building on previously demonstrated magnetic octupole (MOCT)-induced absorption in isolated silicon quadrumers, we examine the periodic structure under normal incidence in free space. The main additional result is an absorption resonance at 785 nm associated with electric quadrupole (EQ) and magnetic quadrupole (MQ) contributions with absorptance above 85% and $Q \approx 95$. The periodic structure also supports an MOCT-associated peak at 892.5 nm with absorptance above 30% and $Q \approx 78$. Cartesian multipole decomposition through the magnetic 16-pole term is used to examine the two resonant responses. The EQ–MQ-associated peak offers stronger absorption and a narrower linewidth, while the MOCT-associated peak has a higher simulated refractive index sensitivity (62.5 versus 25 nm/RIU).

Keywords: dielectric metasurfaces; crystalline silicon; high-order multipole resonances; narrowband absorption; electric and magnetic quadrupoles; magnetic octupole; generalized Kerker effect; refractive index sensing

1. Introduction

High-index nanostructures and metasurfaces have been actively studied in recent decades due to a variety of potential applications [1–3]. Periodic structures based on subwavelength meta-atoms can exhibit interesting properties that are driven by the excitation of electric and magnetic multipole moments. These resonant excitations can be spectrally tuned by changing system parameters like geometry, periodic arrangement and surrounding medium properties [4–7]. The method of multipole decomposition of electromagnetic fields inside the Mie-resonant nanostructures provides a widely used tool for investigating their electromagnetic properties. This approach found its use for both single and periodic structures [8–10].

Due to the scaling properties of Maxwell equations, resonant properties of dielectric structures were studied from nano- to macro-objects [11–13]. In the optical range, dielectric metasurfaces feature chemical stability, nontoxicity, and high refractive index and support Mie resonances, including the higher-order ones [14,15]. Therefore, such nanostructures became a popular choice for many applications such as flat optics [15], structural colors [16], nonlinear photonics [17], holography [18], and sensing [2]. Recently, it was also demonstrated that free-standing metasurfaces can be successfully fabricated and characterized [19–21].

Check for updates

Received: 19 October 2026
Revised: 18 November 2026
Accepted: 25 November 2026
Published: 27 November 2026

Copyright: © 2026 by the authors. Licensee MDPI, Basel, Switzerland. This article is an open access article distributed under the terms and conditions of the Creative Commons Attribution (CC BY) license.

Recent examples include SiC nanobrick metasurfaces for color printing and polarization-dependent information encoding [22], where multipole decomposition identified a dominant magnetic dipole resonance overlapping an electric dipole response in a representative symmetric unit cell. Reflective aluminum nanorod metasurfaces have also been numerically investigated for structural color generation and analyzer-free brightness tuning through orientation-dependent polarization filtering [23]. These dielectric and plasmonic implementations illustrate how the resonant and polarization responses of nanostructures can be tailored for a specific optical function. The present work focuses on higher-order multipole contributions to absorption in c-Si quadrumer metasurfaces.

One of the promising directions is absorbing and accumulating energy from light that could enable smart sensors, solar cells and energy harvesting devices [24,25]. These applications have long been known to benefit from using silicon films [26,27]. However, crystalline silicon (c-Si) poses a unique challenge in the near-infrared (NIR) transparency window, where its indirect bandgap results in extremely low intrinsic absorption [28]. Previous efforts to enhance silicon absorption by nanostructuring have largely focused on the excitation of electric dipole (ED) and magnetic dipole (MD) moments [29,30]. While effective, these dipole-driven mechanisms often reach a performance ceiling in terms of absorption magnitude and spectral selectivity.

We study two absorption resonances in a periodic c-Si quadrumer metasurface under normal-incidence plane wave illumination (Figure 1). Our previous study established magnetic octupole (MOCT) excitation, its gap-dependent tuning, field localization, and resonantly enhanced absorbed power in isolated silicon quadrumers [31]. The present work extends this response to a periodic array, where the MOCT-associated peak exceeds 30% absorption at 892.5 nm. The main additional result is the EQ–MQ-associated absorption peak at 785 nm, which exceeds 85% in this periodic geometry. We used a commercial finite-element numerical solver in the frequency domain and the semi-analytical multipole decomposition approach [6,9] to numerically study the metasurface in free space and analyze the nature of absorption peaks in the near-infrared range. We investigate the two resonant responses and their different absorption linewidths and refractive index sensitivities.

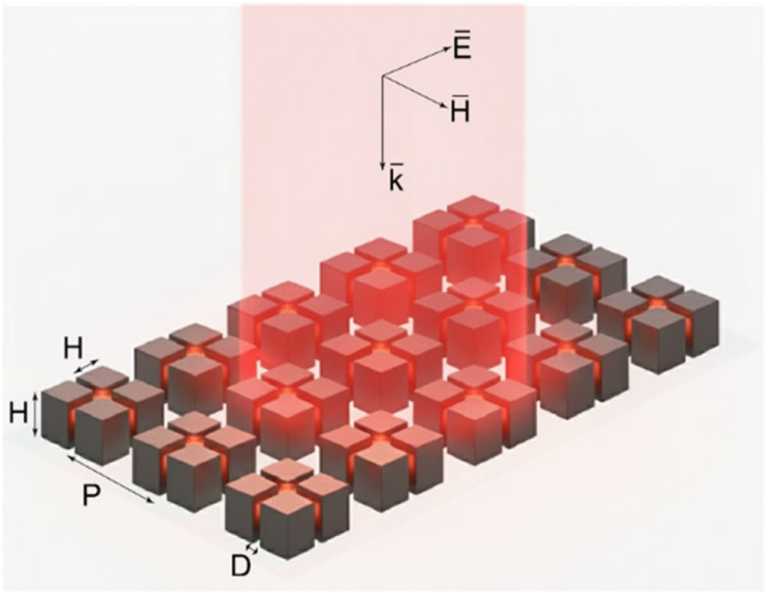

Figure 1. Schematic of the quadrumer-based metasurface and illumination geometry. The quadrumer-based metasurface is illuminated by a plane wave incident normally on the metasurface. The height of each cube is denoted as *H*, quadrumer gap is denoted as *D*, and lattice constant is denoted as *P*.

2. Materials and Methods

We study an idealized metasurface in free space to investigate the fundamental multipolar absorption response. For comparison, we also calculate the direct $R/T/A$ spectra for the same geometry and normal-incidence excitation on a semi-infinite substrate with refractive index $n = 1.4$. In order to analyze the optical properties of a dielectric metasurface, we exploit the semi-analytical multipole decomposition approach [6,9]. First, the total electric fields in quadrumer meta-atoms and corresponding reflectance (R) and transmittance (T) spectra are calculated numerically. The incident port power is 1 W at each wavelength. Then, we implement Cartesian multipole decomposition following Ref. [8]. Multipole contributions are obtained from the electric field integration over the meta-atom volume. The transmittance and reflectance spectra reconstructed from the multipole moments show good agreement with the directly calculated spectra in Figure 2a, supporting the multipole description. For better accuracy compared to a single quadrumer scatterer study [31], here we consider multipoles up to electric and magnetic 16-poles even though the main described effects are found to be quadrupole- and octupole-driven. The absorptance is $A = 1 - R - T$. In the following, we use the described approach to study the pronounced anomalous absorption peaks and analyze the underlying multipole physics.

For the free-space structure at normal incidence, we use the effective electric and magnetic contributions of Ref. [8], denoted P_e and P_m and both expressed in units of electric dipole moment:

$$P_\mathrm{e} = p_\mathrm{x} - \frac{ik_\mathrm{d}M_\mathrm{yz}}{2v_\mathrm{d}} - \frac{k_\mathrm{d}^2 O_\mathrm{xzz}^{(\mathrm{e})}}{6} + \frac{ik_\mathrm{d}^3 S_\mathrm{yzzz}^{(\mathrm{m})}}{24v_\mathrm{d}}$$

$$P_\mathrm{m} = \frac{m_\mathrm{y}}{v_\mathrm{d}} - \frac{ik_\mathrm{d}Q_\mathrm{xz}}{6} - \frac{k_\mathrm{d}^2 O_\mathrm{yzz}^{(\mathrm{m})}}{6v_\mathrm{d}} + \frac{ik_\mathrm{d}^3 S_\mathrm{xzzz}^{(\mathrm{e})}}{24}$$

In the phase convention of the numerical implementation, the reflection and forward-scattered amplitudes, normalized to the incident field, are

$$r = i\alpha(P_\mathrm{e} - P_\mathrm{m}), \quad s_\mathrm{f} = -i\alpha(P_\mathrm{e} + P_\mathrm{m}), \quad t = 1 + s_\mathrm{f}$$

$$\alpha = \frac{k_\mathrm{d}}{2S_\mathrm{L}\varepsilon_0\varepsilon_\mathrm{d}E_0}, \quad R = |r|^2, \quad T = |t|^2$$

Here, S_L is the unit cell area, k_d and v_d are the wavenumber and light velocity in the surrounding medium, and ε_d is its relative permittivity ($\varepsilon_\mathrm{d} = 1$ in air). E_0 is the complex incident electric field at the multipole origin $(0, 0, 0)$; its phase is retained when combining the incident and scattered fields. The moments Q, M, O and S denote the quadrupole, octupole and 16-pole tensors defined in Ref. [8]. The condition $P_\mathrm{e} \approx P_\mathrm{m}$ suppresses reflection and extends the Kerker balance to the higher-order contributions. Low transmission additionally requires the complete forward scattered field to oppose the incident field.

We estimate the spectral quality factor as $Q \approx \lambda_0/\Delta\lambda$, where λ_0 is the absorption peak wavelength and $\Delta\lambda$ is the full width at half maximum (FWHM) of $A(\lambda)$. The two half-maximum wavelengths satisfy $A(\lambda) = A(\lambda_0)/2$ and are obtained by linear interpolation between adjacent points of the 0.5 nm wavelength grid. No background subtraction or lineshape fitting is applied. This linewidth-based Q characterizes the absorption spectrum and does not separate radiative and absorptive decay rates.

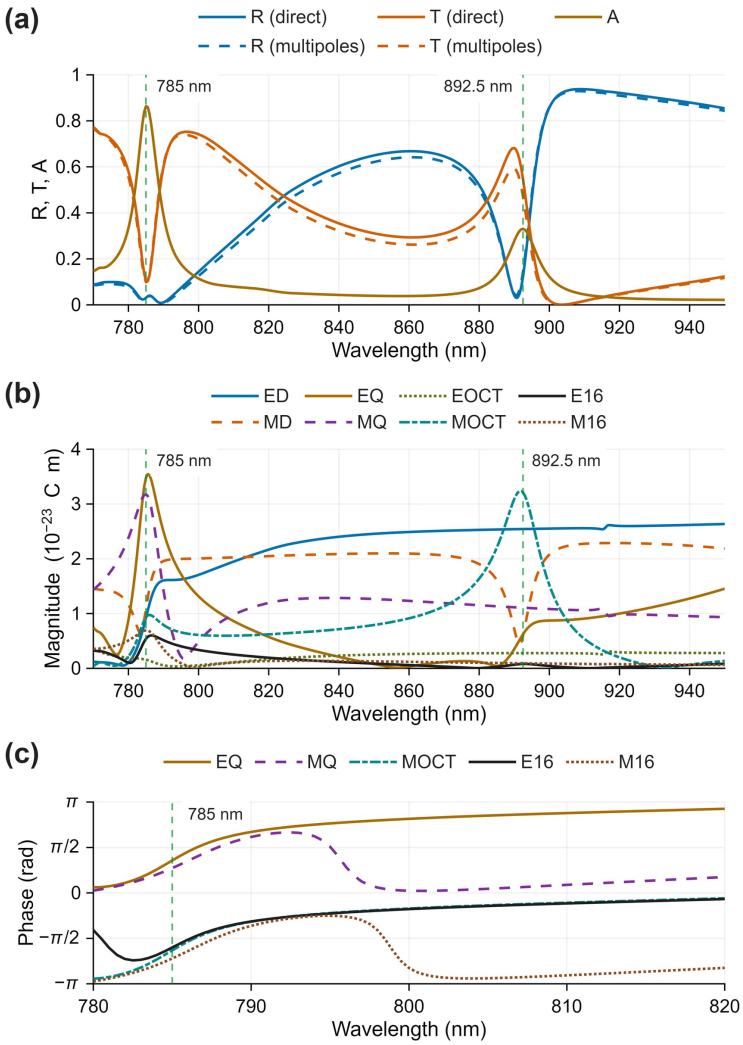

Figure 2. (**a**) The calculated transmittance T, reflectance R and absorptance A for the quadrumer-based silicon metasurface depicted in Figure 1. Dashed lines represent the T and R spectra calculated from multipole contributions. The absorption peaks at 785 and 892.5 nm are marked with green dashed lines. (**b**) Magnitudes of the weighted multipole contributions in common electric dipole units. (**c**) Principal phases near the 785 nm peak (EQ, MQ, MOCT, E16, and M16; 780–820 nm). Colors and line styles identify the same contributions in panels (**b**,**c**). ED/MD denote electric/magnetic dipoles, EQ/MQ quadrupoles, EOCT/MOCT octupoles, and E16/M16 16-poles.

3. Results and Discussion

To explore the narrowband absorption effects, we consider the metasurface that consists of the c-Si quadrumers. Each quadrumer includes four cubes with a height of $H = 250$ nm, the gap between the cubes is $D = 25$ nm, and the metasurface lattice constant is $P = 650$ nm. The cube size and intra-quadrumer gap follow our earlier study of an isolated silicon quadrumer [31]. The lattice constant was chosen to maintain subdiffractive operation at normal incidence in air, $P < \lambda$ throughout the considered wavelength range of 770–950 nm, so no nonzero diffraction orders propagate. The plane wave illumination is set normal to a metasurface plane, as shown with the artistic representation in Figure 1. First, the transmittance, reflectance and absorptance have been calculated over the wavelength range 770–950 nm (Figure 2a). Two absorption peaks are marked with green dashed lines at 785 nm and 892.5 nm. It is important to note that a c-Si film is nearly lossless over this wavelength range, and these peaks are the direct consequence of trapping specific optical modes. To analyze the contribution of multipole moments to the narrowband absorption

effect, as shown in Figure 2b, we calculated the multipole decomposition of the electric field amplitude [8,9].

Let us first consider the peak at $\lambda = 785$ nm. Figure 2b shows that EQ and MQ resonances provide the dominant contributions to the electric field amplitude, while MOCT, electric 16-pole (E16), and magnetic 16-pole (M16) also exhibit weak resonances. The peak exhibits absorption above 85% with FWHM $\Delta\lambda \approx 8.27$ nm and spectral quality factor $Q \approx 95$. Both the absorption and the spectral quality factor exceed those reported for an amorphous silicon (a-Si) MD–ED narrowband absorber on glass in immersion oil ($Q = 11.89$ at 785 nm) [30]. Notably, the intrinsic absorption of a-Si is also substantially higher than that of c-Si [28]. Figure 2c shows the phases of the participating multipole contributions near 785 nm. At 785 nm, the weighted EQ and MQ contributions have a magnitude ratio of 1.095 and a relative phase of 15.2°, while the weaker MOCT, E16 and M16 contributions have different phases. Their effect on the outgoing channels is quantified below.

For backward radiation, the weighted EQ and MQ terms enter with opposite signs. Denoting their normalized reflected-field contributions by r_{EQ} and r_{MQ}, the complex data at 785 nm give

$$\frac{|r_{EQ} + r_{MQ}|^2}{|r_{EQ}|^2 + |r_{MQ}|^2} = 1 + \frac{2\mathrm{Re}\left(r_{EQ} r_{MQ}^*\right)}{|r_{EQ}|^2 + |r_{MQ}|^2} \approx 0.0389$$

Thus, destructive interference reduces the pair's backward power by 96.1% relative to its incoherent sum. This ratio quantifies interference between the two contributions; it is not the total reflectance. Including all multipoles through the magnetic 16-pole gives $R \approx 0.0283$, showing that the weaker contributions also participate in the channel balance.

In the forward scattered field, the EQ and MQ terms add constructively. The complete normalized forward scattered amplitude is $s_f \approx -1.2864 - 0.1288i$, so $t = 1 + s_f \approx -0.2864 - 0.1288i$ and $T \approx 0.0986$. The low transmission therefore results from destructive interference between the incident field and the complete forward scattered field. Together with the backward cancellation, this accounts for the suppressed outgoing channels at a strong absorption resonance. The EQ–MQ cross terms have opposite signs in the two scattered channels and cancel in their sum: they redistribute radiation directionally rather than constitute an independent absorbed-power term. Figure 2a shows good agreement between the reconstructed and directly calculated spectra.

Next, consider the smaller absorption peak at $\lambda = 892.5$ nm. This extendsthat the MOCT-induced absorption and field localization previously demonstrated in isolated quadrumer to a periodic array s [31]. The isolated structure study reports absorbed power in arbitrary units, whereas the present array is characterized by $A = 1 - R - T$. Here, the MOCT-associated peak exceeds 30% absorption with FWHM $\Delta\lambda \approx 11.48$ nm and spectral quality factor $Q \approx 78$. Figure 2b identifies a resonant MOCT contribution near this peak in contrast to the overlapping EQ and MQ resonances near 785 nm.

Figure 3a,b present the characteristic electric field distributions at the wavelengths of 785 nm and 892.5 nm. Both resonances exhibit pronounced electric field hot spots in the quadrumer gaps. For the same incident port power, the electric field magnitude is higher at 785 nm (Figure 3a). In turn, Figure 3c,d exhibit the magnetic field distribution in a meta-atom. While the field distribution in Figure 3d resembles the MOCT-associated distribution reported for a single meta-atom [31] and shows similar magnetic hot spots, Figure 3c shows a more complex pattern at the EQ–MQ-associated resonance. Unlike the MOCT-associated pattern in Figure 3d, Figure 3c does not exhibit comparable magnetic field hot spots in the gaps.

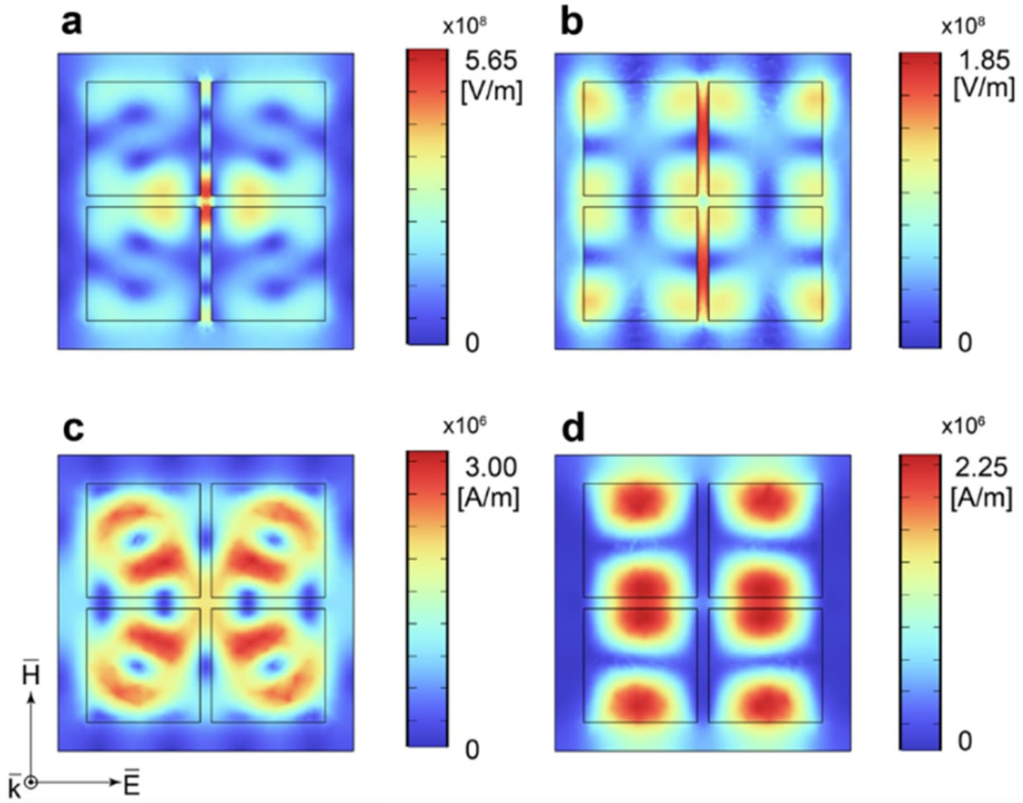

Figure 3. (**a**,**b**) Distributions of the electric field magnitude in the 650 nm unit cell in the (xy) plane ($z = 0$) of the silicon quadrumer meta-atom in a periodic structure. (**a**) $\lambda = 785$ nm; (**b**) $\lambda = 892.5$ nm. (**c**,**d**) Distributions of the magnetic field absolute value in the same plane. (**c**) $\lambda = 785$ nm; (**d**) $\lambda = 892.5$ nm. FEM normE and normH are shown in V/m and A/m, respectively, for 1 W incident port power in the same simulations as the R/T/A spectra. The maps are not divided by incident field amplitudes; color bar scales differ between panels.

Published isolated-particle results provide context for the two array resonances. For an isolated silicon cube with a 250 nm edge, Ref. [4] reports EQ scattering resonances at 619 and 704 nm and an MQ resonance at 765 nm, all at shorter wavelengths than the array peak at 785 nm. Comparable dipolar and quadrupolar contributions also produce side scattering near 793 nm in the isolated cube [4]. An isolated quadrumer with the present cube size and 25 nm gaps already supports an MOCT resonance near 874 nm [31]; this response therefore does not require a periodic lattice. The present array exhibits overlapping EQ and MQ contributions near 785 nm and an MOCT-associated absorption peak at 892.5 nm. The resonance positions and multipolar overlap can be further controlled through particle height tuning [4], variation of the intra-quadrumer gap [31], and changes in the array period [9]. These established geometrical controls provide routes to tailor the absorption response beyond the representative geometry considered here.

Next, we consider one of the potential application scenarios to additionally showcase the difference between two absorption enhancement mechanisms. Here, we numerically vary the refractive index of the entire surrounding medium, including the quadrumer gaps, to study the shifts of the two resonances. Such an analysis is relevant to refractive index sensing and is widely applicable in biomedicine and other areas [32]. As shown in Figure 4, both resonances redshift as the refractive index increases. However, the MOCT resonance (Figure 4b) experiences a larger shift than the combined EQ–MQ resonance (Figure 4a). Previously, it was shown that electric multipoles are more sensitive to refractive index changes than their magnetic counterparts of the same order [33]. For the present geometry, the MOCT-associated peak has a simulated sensitivity of 62.5 nm per refractive

index unit (RIU) compared with 25 nm/RIU for the EQ–MQ-associated resonance. The MOCT sensitivity is comparable to values reported for microdisk laser and plasmonic fiber sensors [34,35] although lower than those reported for sensors based on quasi-bound states in the continuum (quasi-BICs) in Refs. [36,37]. Table 1 compares the calculated absorption and sensing metrics of the two resonances. A small-angle comparison is discussed below.

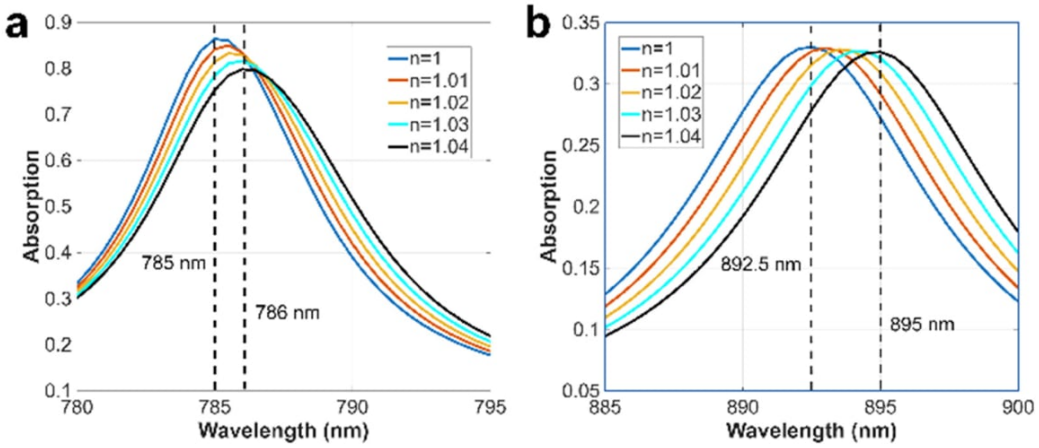

Figure 4. Redshift of the (**a**) EQ–MQ and (**b**) MOCT resonances with increasing refractive index of the surrounding medium. The MOCT-associated peak exhibits the larger wavelength shift over the simulated refractive index range.

Table 1. Comparison of the two absorption resonances in the periodic c-Si quadrumer metasurface.

Quantity	EQ–MQ-Associated Peak	MOCT-Associated Peak
Resonant contributions (Figure 2b)	Overlapping EQ and MQ	Pronounced MOCT
Peak wavelength (nm)	785	892.5
Peak absorptance (%)	86.3	33.0
FWHM $\Delta\lambda$ (nm)	8.27	11.48
Spectral Q	95	78
Sensitivity S (nm/RIU)	25	62.5
FOM (RIU^{-1})	3.02	5.45

Values refer to normal incidence and use the absorption linewidths at $n = 1$. Absorptance, FWHM and Q are obtained from the total absorption spectrum in Figure 2a; S is the simulated sensitivity reported in Figure 4. FOM = $S/\Delta\lambda$ uses the unrounded linewidths.

To compare field exposure to the surrounding medium at $n = 1$, we integrate $|E|^2$ and $|H|^2$ over the four silicon cubes and the air portion of one unit cell within $-125 \leq z \leq 125$ nm, including the gaps. For each field, the local air fraction is the air integral divided by the sum of the air and silicon integrals. At 785 and 892.5 nm, the electric field fractions are 37.2% and 50.8%, respectively; the corresponding magnetic field fractions are 13.1% and 14.1%. The larger relative electric field exposure of the MOCT-associated resonance is consistent with its greater sensitivity to the surrounding refractive index. These unweighted finite-volume fractions characterize the local field distribution; they are not modal energy fractions and do not provide a quantitative perturbation theory prediction of the sensitivities.

The resonances differ in their dominant spectral contributions: overlapping EQ and MQ resonances at 785 nm and a pronounced MOCT resonance at 892.5 nm (Figure 2b). Within the simulated geometry, the first peak provides higher absorptance and a narrower

absorption linewidth, while the second gives a larger wavelength shift per refractive index change. For wavelength shift sensing, we define the spectral figure of merit as FOM = $S/\Delta\lambda$, where S is the sensitivity from Figure 4 and $\Delta\lambda$ is the absorption FWHM at $n = 1$. This gives approximately 3.02 and 5.45 RIU^{-1} for the 785 and 892.5 nm peaks, respectively. These spectral metrics do not by themselves establish a detection limit.

With a semi-infinite $n = 1.4$ substrate, the direct spectra retain absorption features near 786 and 922 nm with sampled peak absorptances of approximately 30.4% and 26.0%, respectively, compared with 86.3% and 33.0% in free space. The qualitative inspection of the multipole spectra is consistent with persistence of the EQ–MQ- and MOCT-associated responses, respectively, although the spectrum is modified. The free-space multipolar R/T formulas are not applied to this supported geometry.

For p-polarized illumination at 2° elevation and 0° azimuth, additional free-space calculations retain the two principal absorption peaks with sampled maxima of 83.9% at 786 nm and 32.8% at 892 nm. The sampled normal-incidence maxima are 83.2% and 32.8%, respectively. Thus, the two principal peaks are preserved under this tilt, confirming small-angle robustness.

To estimate the radiative and absorptive loss balance near 785 nm, we fit the complex normal-incidence S parameters from port planes $z = \pm 500$ nm that are referred to $z = 0$. For the mirror-symmetric free-space array, the channels in a common transverse electric field basis are $s_{\pm} = r_S \pm t_S$. The multipole reconstruction in this basis is $r_S = -r$ and $t_S = t$, where r and t are defined in Section 2. Symmetric and antisymmetric refer to reflection through the metasurface plane $z = 0$. For the multipole components excited at normal incidence, the MQ contribution belongs to the symmetric radiation channel, whereas the EQ contribution belongs to the antisymmetric channel. Their spectral overlap therefore connects the multipolar interpretation near 785 nm with the strong absorption in both scattering channels. The MOCT contribution near 892.5 nm also belongs to the antisymmetric channel. The fitted decay rates characterize each complete scattering channel, including its other allowed multipole contributions. Over 776–796 nm, each channel is represented by an effective single-resonance model:

$$s_\sigma(\omega) = b_\sigma(\omega)[1 - \frac{2\gamma_{r,\sigma}}{\gamma_{r,\sigma} + \gamma_{a,\sigma} + i(\omega - \omega_\sigma)}]$$

Here, $\sigma = +$ or $-$ labels the channel; $\gamma_{r,\sigma}$ and $\gamma_{a,\sigma}$ are positive radiative and absorptive amplitude decay rates. The passive background b_σ has a log magnitude that is linear in frequency and a quadratic phase. The fitted resonance wavelengths are 786.27 and 784.69 nm with radiative-to-absorptive rate ratios of approximately 2.4 and 1.55, respectively. Both channels are radiatively overcoupled; the antisymmetric channel is closer to critical coupling, where the rates are equal. At 785 nm, the channel absorptances are 77.9% and 94.8%, whose mean gives 86.3% for one-sided illumination. These effective model estimates support spectral overlap of two dissipative channels without establishing exact critical coupling. They are distinct from the linewidth-based spectral Q reported above.

4. Conclusions

This study extends the analysis of isolated silicon quadrumers to the absorption spectra of a periodic c-Si metasurface and compares an EQ–MQ-associated resonance with the previously established MOCT response. Our analysis, supported by the Cartesian multipole decomposition extended to the 16-pole term, identifies two distinct resonant regimes within the near-infrared transparency window of crystalline silicon.

The principal additional result is the EQ–MQ-associated absorption peak at 785 nm with absorptance above 85% and $Q \approx 95$. The MOCT-associated peak at 892.5 nm extends the

earlier isolated-quadrumer response to the periodic array with absorptance above 30% and $Q \approx 78$. Within this common geometry, the EQ–MQ-associated peak has higher absorptance and a narrower linewidth, whereas the MOCT-associated peak has higher refractive index sensitivity and a larger sensing figure of merit. The channel analysis shows that the nearly in-phase EQ and MQ contributions suppress backward radiation, while the complete forward scattered field interferes with the incident wave to reduce transmission. The literature comparison relates these array resonances to the local multipolar responses of an isolated cube and quadrumer [4,31]. The $n = 1.4$ substrate comparison retains identifiable resonant features with reduced absorption relative to free space at normal incidence. Both principal free-space peaks remain pronounced for the tested p-polarized tilt of 2° at 0° azimuth.

Author Contributions: P.T.: conceptualization (lead); methodology (lead); formal analysis (lead); investigation (lead); visualization (lead); writing—original draft (lead); writing—review and editing (supporting). V.A.: investigation (supporting); writing—review and editing (supporting); funding acquisition (lead). All authors have read and agreed to the published version of the manuscript.

Funding: This work was performed under financial assistance award 70NANB24H152 from the National Institute of Standards and Technology, U.S. Department of Commerce. The statements, findings, conclusions, and recommendations are those of the authors and do not necessarily reflect the views of the National Institute of Standards and Technology or the U.S. Department of Commerce.

Data Availability Statement: The data that support the findings of this study are available from the corresponding author upon reasonable request.

Conflicts of Interest: The authors declare no conflicts of interest.

References

1. Faraz, F.; Tian, J.; Abbasi, T.U.R.; Zhu, W. Recent Advances in Geometric Phase Metasurfaces: Principles and Applications. *Adv. Phys. Res.* **2025**, *4*, 2400095. [CrossRef]
2. Chung, T.; Wang, H.; Cai, H. Dielectric metasurfaces for next-generation optical biosensing: A comparison with plasmonic sensing. *Nanotechnology* **2023**, *34*, 402001. [CrossRef] [PubMed]
3. Sharapova, P.R.; Kruk, S.S.; Solntsev, A.S. Nonlinear Dielectric Nanoresonators and Metasurfaces: Toward Efficient Generation of Entangled Photons. *Laser Photon. Rev.* **2023**, *17*, 2200408. [CrossRef]
4. Terekhov, P.D.; Baryshnikova, K.V.; Artemyev, Y.A.; Karabchevsky, A.; Shalin, A.S.; Evlyukhin, A.B. Multipolar response of nonspherical silicon nanoparticles in the visible and near-infrared spectral ranges. *Phys. Rev. B* **2017**, *96*, 035443. [CrossRef]
5. Basharin, A.A.; Kafesaki, M.; Economou, E.N.; Soukoulis, C.M.; Fedotov, V.A.; Savinov, V.; Zheludev, N.I. Dielectric metamaterials with toroidal dipolar response. *Phys. Rev. X* **2015**, *5*, 011036. [CrossRef]
6. Ustimenko, N.; Rockstuhl, C.; Evlyukhin, A.B. Resonances in finite-size all-dielectric metasurfaces for light trapping and propagation control. *Phys. Rev. B* **2024**, *109*, 115436. [CrossRef]
7. Sakhare, P.A.; Atmakuri, M.; Dontabhaktuni, J. Tailoring the resonant modes in liquid crystal based all-dielectric metasurfaces. *Sci. Rep.* **2023**, *13*, 6780. [CrossRef] [PubMed]
8. Allayarov, I.; Evlyukhin, A.B.; Lesina, A.C. Multiresonant all-dielectric metasurfaces based on high-order multipole coupling in the visible. *Opt. Express* **2024**, *32*, 5641–5658. [CrossRef] [PubMed]
9. Terekhov, P.D.; Babicheva, V.E.; Baryshnikova, K.V.; Shalin, A.S.; Karabchevsky, A.; Evlyukhin, A.B. Multipole analysis of dielectric metasurfaces composed of non-spherical nanoparticles and lattice invisibility effect. *Phys. Rev. B* **2019**, *99*, 045424. [CrossRef]
10. Krasikov, S.; Odit, M.; Dobrykh, D.; Yusupov, I.; Mikhailovskaya, A.; Shakirova, D.; Shcherbakov, A.; Slobozhanyuk, A.; Ginzburg, P.; Filonov, D.; et al. Multipolar Engineering of Subwavelength Dielectric Particles for Scattering Enhancement. *Phys. Rev. Appl.* **2021**, *15*, 024052. [CrossRef]
11. Han, A.; Moloney, J.V.; Babicheva, V.E. Applicability of multipole decomposition to plasmonic- and dielectric-lattice resonances. *J. Chem. Phys.* **2022**, *156*, 114104. [CrossRef] [PubMed]
12. Terekhov, P.D.; Baryshnikova, K.V.; Evlyukhin, A.B.; Shalin, A.S. Destructive interference between electric and toroidal dipole moments in TiO2 cylinders and frustums with coaxial voids. *J. Phys. Conf. Ser.* **2017**, *929*, 012065. [CrossRef]
13. Balezin, M.; Baryshnikova, K.V.; Kapitanova, P.; Evlyukhin, A.B. Electromagnetic properties of the Great Pyramid: First multipole resonances and energy concentration. *J. Appl. Phys.* **2018**, *124*, 034903. [CrossRef]

14. Prokhorov, A.V.; Terekhov, P.D.; Gubin, M.Y.; Shesterikov, A.V.; Ni, X.; Tuz, V.R.; Evlyukhin, A.B. Resonant Light Trapping via Lattice-Induced Multipole Coupling in Symmetrical Metasurfaces. *ACS Photonics* **2022**, *9*, 3869–3875. [CrossRef]
15. Zenin, V.A.; Garcia-Ortiz, C.E.; Evlyukhin, A.B.; Yang, Y.; Malureanu, R.; Novikov, S.M.; Coello, V.; Chichkov, B.N.; Bozhevolnyi, S.I.; Lavrinenko, A.V.; et al. Engineering Nanoparticles with Pure High-Order Multipole Scattering. *ACS Photonics* **2020**, *7*, 1067–1075. [CrossRef]
16. Wang, L.; Wang, T.; Yan, R.; Yue, X.; Wang, H.; Wang, Y.; Zhang, J.; Yuan, X.; Zeng, J.; Wang, J. Color Printing and Encryption with Polarization-Switchable Structural Colors on All-Dielectric Metasurfaces. *Nano Lett.* **2023**, *23*, 5581–5587. [CrossRef] [PubMed]
17. Wang, Z.; Lin, R.; Yao, J.; Tsai, D.P. All-dielectric nonlinear metasurface: From visible to vacuum ultraviolet. *npj Nanophoton* **2025**, *2*, 4. [CrossRef]
18. Ding, Y.; Chen, X.; Duan, Y.; Huang, H.; Zhang, L.; Chang, S.; Guo, X.; Ni, X. Metasurface-Dressed Two-Dimensional on-Chip Waveguide for Free-Space Light Field Manipulation. *ACS Photonics* **2022**, *9*, 398–404. [CrossRef] [PubMed]
19. Sirmaci, Y.D.; Tang, Z.; Fasold, S.; Neumann, C.; Pertsch, T.; Turchanin, A.; Staude, I. Plasmonic Metasurfaces Situated on Ultrathin Carbon Nanomembranes. *ACS Photonics* **2020**, *7*, 1060–1066. [CrossRef]
20. Tseng, M.L.; Leitis, A.; John-Herpin, A.; Kivshar, Y.S.; Altug, H. Wafer-Scale Functional Metasurfaces on Free-Standing Membranes. In *Proceedings of the Conference on Lasers and Electro-Optics*; Paper FM4F.5; IEEE: New York, NY, USA, 2022.
21. Dorrah, A.H.; Park, J.S.; Palmieri, A.; Capasso, F. Free-standing bilayer metasurfaces in the visible. *Nat. Commun.* **2025**, *16*, 3126. [CrossRef] [PubMed]
22. Ren, Y.; Jin, R.; Song, M.; Lin, P.; Xu, T.; Lu, Y.-Q. High-Performance Color Printing and Information Encryption Enabled by Silicon Carbide Metasurface. *Adv. Funct. Mater.* **2016**, *36*, e26191. [CrossRef]
23. Ren, Y.; Liu, G.; Zhang, Y.; Gao, L. Analyzer-Free and Brightness-Tuning Structural Color Enabled by Reflective Malus-Assisted Metasurface. *Photonics* **2026**, *13*, 986. [CrossRef]
24. Mascaretti, L.; Chen, Y.; Henrotte, O.; Yesilyurt, O.; Shalaev, V.M.; Naldoni, A.; Boltasseva, A. Designing Metasurfaces for Efficient Solar Energy Conversion. *ACS Photonics* **2023**, *10*, 4079–4103. [CrossRef] [PubMed]
25. Cortés, E.; Wendisch, F.J.; Sortino, L.; Mancini, A.; Ezendam, S.; Saris, S.; de S Menezes, L.; Tittl, A.; Ren, H.; Maier, S.A. Optical Metasurfaces for Energy Conversion. *Chem. Rev.* **2022**, *122*, 15082–15176. [CrossRef] [PubMed]
26. Redfield, D. Multiple-pass thin-film silicon solar cell. *Appl. Phys. Lett.* **1974**, *25*, 647–648. [CrossRef]
27. Carlson, D.E.; Wronski, C.R. Amorphous silicon solar cells. *Appl. Phys. Lett.* **1976**, *28*, 671–673. [CrossRef]
28. Palik, E.D. *Handbook of Optical Constants of Solids, Five-Volume Set: Handbook of Thermo-Optic Coefficients of Optical Materials with Applications*; Elsevier: Amsterdam, The Netherlands, 1997.
29. Terekhov, P.D.; Baryshnikova, K.V.; Greenberg, Y.; Fu, Y.H.; Evlyukhin, A.B.; Shalin, A.S.; Karabchevsky, A. Enhanced absorption in all-dielectric metasurfaces due to magnetic dipole excitation. *Sci. Rep.* **2019**, *9*, 3438. [CrossRef] [PubMed]
30. Yang, C.Y.; Yang, J.H.; Yang, Z.Y.; Zhou, Z.X.; Sun, M.G.; Babicheva, V.E.; Chen, K.P. Nonradiating Silicon Nanoantenna Metasurfaces as Narrowband Absorbers. *ACS Photonics* **2018**, *5*, 2596–2601. [CrossRef]
31. Terekhov, P.D.; Evlyukhin, A.B.; Redka, D.; Volkov, V.S.; Shalin, A.S.; Karabchevsky, A. Magnetic Octupole Response of Dielectric Quadrumers. *Laser Photon. Rev.* **2020**, *14*, 1900331. [CrossRef]
32. Sun, S.; Wu, L.; Geng, Z.; Shum, P.P.; Ma, X.; Wang, J. Refractometric Imaging and Biodetection Empowered by Nanophotonics. *Laser Photon. Rev.* **2023**, *17*, 2200814. [CrossRef]
33. Terekhov, P.D.; Shamkhi, H.K.; Gurvitz, E.A.; Baryshnikova, K.V.; Evlyukhin, A.B.; Shalin, A.S.; Karabchevsky, A. Broadband forward scattering from dielectric cubic nanoantenna in lossless media. *Opt. Express* **2019**, *27*, 10924–10935. [CrossRef] [PubMed]
34. Jeong, H.; Park, N.R.; Park, B.J.; Kim, M.; Kim, J.T.; Kim, M.K. Highly sensitive microdisk laser sensor for refractive index sensing via periodic meta-hole patterning. *Nanophotonics* **2025**, *14*, 1193–1202. [CrossRef] [PubMed]
35. Chah, K.; Voisin, V.; Kinet, D.; Caucheteur, C. Surface plasmon resonance in eccentric femtosecond-laser-induced fiber Bragg gratings. *Opt. Lett.* **2014**, *39*, 6887–6890. [CrossRef] [PubMed]
36. Hsiao, H.H.; Hsu, Y.C.; Liu, A.Y.; Hsieh, J.C.; Lin, Y.H. Ultrasensitive Refractive Index Sensing Based on the Quasi-Bound States in the Continuum of All-Dielectric Metasurfaces. *Adv. Opt. Mater.* **2022**, *10*, 2200812. [CrossRef]
37. Luo, M.; Zhou, Y.; Zhao, X.; Guo, Z.; Li, Y.; Wang, Q.; Liu, J.; Luo, W.; Shi, Y.; Liu, A.Q.; et al. High-Sensitivity Optical Sensors Empowered by Quasi-Bound States in the Continuum in a Hybrid Metal–Dielectric Metasurface. *ACS Nano* **2024**, *18*, 6477–6486. [CrossRef] [PubMed]

Disclaimer/Publisher's Note: The statements, opinions and data contained in all publications are solely those of the individual author(s) and contributor(s) and not of MDPI and/or the editor(s). MDPI and/or the editor(s) disclaim responsibility for any injury to people or property resulting from any ideas, methods, instructions or products referred to in the content.